Materials Today Communications 54 (2026) 115539

Contents lists available at ScienceDirect

Materials Today Communications

journal homepage: www.elsevier.com/locate/mtcomm

High-temperature capacitance stability and insulating properties of PNb_9O_{25} synthesized via liquid-phase sintering: Strategic utilization of glass-oxide interfacial reactions

Keisuke Shimamura *, Daisuke Ogawa, Chihaya Fujiwara, Hiromasa Namiki, Naoki Tachibana

Tokyo Metropolitan Industrial Technology Research Institute, 2-4-10, Aomi, Koto-ku, Tokyo 135-0064, Japan

ARTICLE INFO

Keywords:
PNb_9O_{25}
Dielectric materials
Dielectric properties
Liquid-phase sintering
Wadsley–Roth phase
High temperature capacitance stability

ABSTRACT

High-performance dielectric materials are essential for production of electrical storage capacitors used in electric vehicles, solar converters, and aerospace power conditioning applications where power systems and electronic devices must operate reliably at elevated temperatures. This study investigates PNb_9O_{25} as a high-temperature dielectric material and reports our liquid-phase sintering method that utilizes interfacial reactions between SiO_2–P_2O_5 glasses and Nb_2O_5 to form PNb_9O_{25} with SiO_2-rich amorphous boundaries. The synthesized SiO_2–PNb_9O_{25} composites show a denser microstructure than PNb_9O_{25} synthesized through the solid-state reaction. PNb_9O_{25} synthesized via our liquid-phase sintering approach exhibits a high dielectric constant (376), superior high-temperature capacitance stability (within ±15% up to 300 °C), and low electrical conductivity ($\leq 10^{-7}$ S cm^{-1} below 300 °C). These high-temperature capacitance stability and insulating properties are attributed to its amorphous–crystalline microstructure, where SiO_2–rich amorphous phase performs multiple functions, including the suppression of grain growth and oxygen-vacancy formation. SiO_2–PNb_9O_{25} composites synthesized using our liquid-phase sintering method are promising materials for high-temperature dielectric applications.

1. Introduction

The advancement of electrical storage devices used in high-temperature environments, such as those in electric vehicles, aerospace, and military equipment, requires dielectric materials that can maintain a high dielectric constant (high energy density), low capacitance variation, and good insulating properties over a wide temperature range extending to 200 °C or even 300 °C [1–4]. So far, relaxor dielectric materials are mostly based on perovskite-structured solid solutions, such as (Ba,Ca)TiO_3, (K,Na)NbO_3, and (Bi, Na)TiO_3, as end members and have been reported to exhibit good dielectric temperature stability [5–7]. These dielectric materials with highly stable capacitance over a wide temperature range have been prepared by combining multiple perovskite-structured dielectric materials and optimizing their compositions. However, combining multiple perovskite-structured solid solutions leads to compositional complexity, and the volatility of alkali components further hinders the synthesis of high-quality, dense dielectric materials.

Recently, Wadsley–Roth phase PNb_9O_{25} synthesized using spark plasma sintering (SPS) method has been reported to exhibit a high dielectric constant (> 1000), low dielectric loss, and good thermal stability, indicating that PNb_9O_{25}-based materials are promising candidates for high-temperature dielectric applications [8]. Although the crystal structure of PNb_9O_{25} was determined in the 1960s, studies on its physical properties remained scarce until the 2000s [9,10]. To the best of our knowledge, the referenced above report was the first report on the dielectric properties of PNb_9O_{25} [8]. In addition, the study indicated that controlling oxygen vacancies remains challenging, as synthesis via SPS method can reduce Nb, necessitating post-annealing in an oxygen atmosphere. At the same time, the presence of oxygen vacancies can degrade capacitance stability and insulating properties at elevated temperatures. The dielectric properties of PNb_9O_{25} synthesized via the solid-state reaction method, which is commonly used in the fabrication of multilayer ceramic capacitors, have also been reported [11]. In addition to Nb reduction and rapid grain growth during sintering, solid-state reaction method yields a coarse-grained microstructure,

* Corresponding author.
E-mail address: shimamura.keisuke@iri-tokyo.jp (K. Shimamura).

https://doi.org/10.1016/j.mtcomm.2026.115539
Received 19 April 2026; Received in revised form 31 May 2026; Accepted 10 June 2026
Available online 11 June 2026

which increases dielectric loss and degrades dielectric stability at elevated temperatures.

Superior insulating properties and low dielectric loss typically originate from a dense and fine-grained microstructure. Glass–ceramics, synthesized through glass crystallization, consist of dielectric crystals surrounded by amorphous phases, a microstructure that can achieve excellent insulation [12–14]. However, their dielectric constant is relatively low due to the low volume fraction of the dielectric crystals and the precipitation of secondary phases. To overcome these limitations, the volume fraction of the dielectric crystals should be increased and the formation of undesirable secondary phases should be minimized.

To increase the volume fraction of target dielectric crystals and form an amorphous–crystalline microstructure, we utilized interfacial reactions between glasses and oxides during liquid-phase sintering. Conventional liquid-phase sintering is widely used for the fabrication of low-temperature co-fired ceramics (LTCC), in which pre-synthesized dielectric crystals are combined with low-melting glasses to reduce the sintering temperature (Fig. 1**(a)**). Low-melting glasses are typically multicomponent systems designed to possess a low melting points, which increases the number of possible reaction pathways with dielectric crystals and promotes the formation of secondary phases. For example, multiple impurity phases, including $BaTi(BO_3)_2$ and $MgLaB_5O_{10}$, are formed during the liquid-phase sintering of $BaTi_4O_9$ using B_2O_3–La_2O_3–MgO–TiO_2 glasses [15]. Thus, suppressing the precipitation of secondary phases requires appropriately design of both the glass composition and the synthesis method. In contrast to conventional liquid-phase sintering, in our approach, the target crystalline phase is synthesized through glass–oxide interfacial reactions owing to the design of glass compositions and the overall system composition based on the reaction pathways (Fig. 1**(b)**). We expected that the formation of the target crystalline phase and a microstructure consisting of grains bonded by amorphous phases can enhance grain-boundary resistance, improving capacitance stability and insulating properties at elevated temperature. In the present paper, PNb_9O_{25} was synthesized via interfacial reactions between precursor glass and raw oxide, and its microstructure, as well as dielectric and electrical properties, were investigated.

2. Experimental procedures

2.1. Synthesis of precursor glass and characterization

The nominal composition of the melt-quenched sample synthesized in this study was $50SiO_2$–$50\ P_2O_5$. Commercial powders of reagent-grade SiO_2 and $NH_4H_2PO_4$ were mixed and melted in an alumina crucible at 1400 °C for 20 min in an electric furnace. The melt was cooled to room temperature by removing the crucible from the electric furnace and placing it on a firebrick. The endothermic dip due to the glass transition (T_g), the exothermic peak due to crystallization (T_p), and the endothermic peak due to melting (T_m) were determined using differential thermal analysis (DTA; Burker AXS TG-DTA2020SA) at a heating rate of 10 K min^{-1}.

2.2. Synthesis of PNb_9O_{25} and characterization

The nominal compositions of the samples, together with the synthesis method and crystalline phases, were summarized in Table 1. PNb_9O_{25} was synthesized using both liquid-phase sintering and solid-state reaction methods, as shown in Figure S1. For the sample synthesized through liquid-phase sintering, the composition was designed based on the stoichiometry of PNb_9O_{25} using a mixture of $50SiO_2$–$50\ P_2O_5$ glass powder and Nb_2O_5. Commercial powders of reagent-grade Nb_2O_5 and $50SiO_2$–$50\ P_2O_5$ glass powder (prepared in a previous process as precursor glass) were weighed and mixed through ball milling for 24 h using ethanol and zirconia balls. After drying, the mixture was compacted through biaxial pressing at 20 MPa for 2 min, followed by cold isostatic pressing at 250 MPa for 5 min, and then sintered at 1300 °C for 5 h (Figure S1**(a)**). The sample of stoichiometric PNb_9O_{25} was synthesized via the solid-state reaction. Commercial powders of reagent-grade $NH_4H_2PO_4$ and Nb_2O_5 were weighed and mixed through ball milling for 12 h using ethanol and zirconia balls. After drying, the mixture was calcined at 1000 °C for 2 h, followed by pulverization via ball milling for 24 h using ethanol and zirconia balls. After drying, the calcined mixture was compacted using biaxial pressing at 20 MPa for 2 min, followed by cold isostatic pressing at 250 MPa for 5 min, and then sintered at 1300 °C for 5 h (Figure S1**(b)**).

The apparent densities were measured using the Archimedes method, with distilled water as an immersion liquid. In addition, the true densities of the samples after pulverization were measured using a He pycnometer (Shimazu AccuPycII). The crystal structures and chemical states were analyzed via XRD (Rigaku SmartLab, Cu Kα) and XPS (Kratos Ultra2, Al Kα) at room temperature, respectively. The microstructure was observed using the field emission-scanning electron microscopy (FE-SEM; Hitachi High-Tech SU8600) coupled with the energy dispersive X-ray spectrometer (Oxford Ultim Extreme and Ultim Max 100). The local structures of the grains and grain boundaries were observed using a transmission electron microscope (TEM; FEI Titan Cubed G2 60-300). The dielectric and electrical properties were characterized using an LCR meter (Keysight E4980A) and the pyZwx impedance analysis software [16]. As electrode, gold films were sputtered on both sides using a quick coater (Sanyu Denshi SC−701AT).

Table 1
Compositions and crystalline phases of the samples synthesized via the solid-state reaction and liquid-phase sintering.

Compositions (mol. %)			Crystalline phase	Synthesis method
SiO_2	P_2O_5	Nb_2O_5		
	10	90	PNb_9O_{25}	Solid-state reaction
9.1	9.1	81.8	PNb_9O_{25}	Liquid-phase sintering

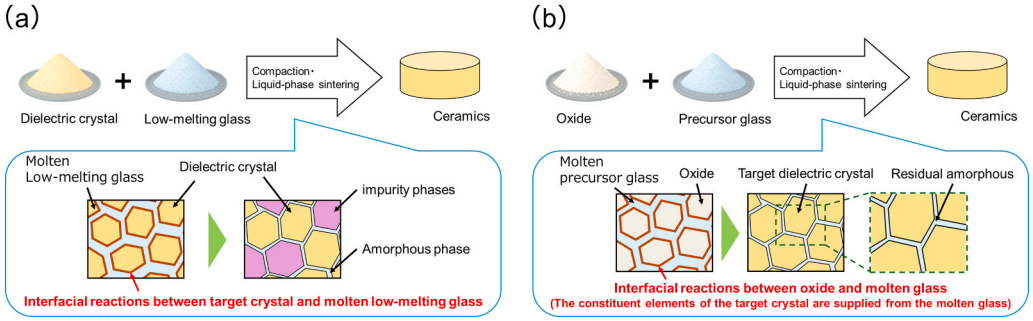

Fig. 1. Schematic diagram of the (a) conventional liquid-phase sintering and (b) our liquid-phase sintering approach.

3. Results and discussion

3.1. Glass formation and thermal properties of precursor glass

The obtained 50SiO_2–50 P_2O_5 sample was optically transparent, and XRD analysis confirmed that it was amorphous as shown in Fig. 2**(a)**. The DTA profile for the 50SiO_2–50 P_2O_5 glass sample is shown in Fig. 2 **(b)**. The glass transition temperature (T_g), crystallization temperature (T_p), and melting point (T_m) were 622, 860, 1243 °C, respectively. The optical photographs before and after heat treatment are provided in Fig. 2**(b)**. The 50SiO_2–50 P_2O_5 glass powder formed a liquid phase during heat treatment at 1300 °C for 5 h under the same conditions as liquid-phase sintering, yielding a glassy sample.

3.2. Synthesis of PNb_9O_{25} and its microstructure

The powder X-ray diffraction (XRD) patterns of the samples synthesized via the solid-state reaction and liquid-phase sintering, together with a theoretical pattern of PNb_9O_{25} calculated from the pristine PNb_9O_{25} crystal structure [9], are shown in Fig. 3. PNb_9O_{25} crystals having a tetragonal structure were obtained via both solid-state reaction and liquid-phase sintering.

The measured apparent densities at room temperature of the samples synthesized through the solid-state reaction and liquid-phase sintering were 4.1 g cm^{-3} and 4.0 g cm^{-3}, respectively. The corresponding true densities were 4.56 g cm^{-3} and 4.35 g cm^{-3}. The true density of the sample synthesized using the solid-state reaction is in good agreement with values reported in previous study [9]. The lower true density of the sample synthesized via liquid-phase sintering, compared with that synthesized via the solid-state reaction, can be attributed to the presence of amorphous phases in addition to PNb_9O_{25}. The relative densities of the samples synthesized via the solid-state reaction and liquid-phase sintering, calculated as the ratio of the apparent density to the true density, were 89% and 93%, respectively. The higher relative density of the liquid-phase sintered sample compared with the solid-state sintered sample can be attributed to the wetting of Nb_2O_5 particles by the molten 50SiO_2–50 P_2O_5 glass during sintering, which generates capillary forces that enhance dentification [17].

Fig. 4**(a)** and **(b)** show scanning electron microscopy (SEM) photographs of the fracture surface of PNb_9O_{25} samples synthesized via the solid-state reaction and liquid-phase sintering, respectively. The samples synthesized through the solid-state reaction and liquid-phase sintering exhibit different microstructures. In the PNb_9O_{25} synthesized using the solid-state reaction, the grain size is larger than 20 μm, and numerous intragranular pores with sizes of ≤ 1 μm are observed. In contrast, the grain size of PNb_9O_{25} synthesized via liquid-phase sintering is ≤ 10 μm, with pores mainly present at grain boundaries and triple junctions of

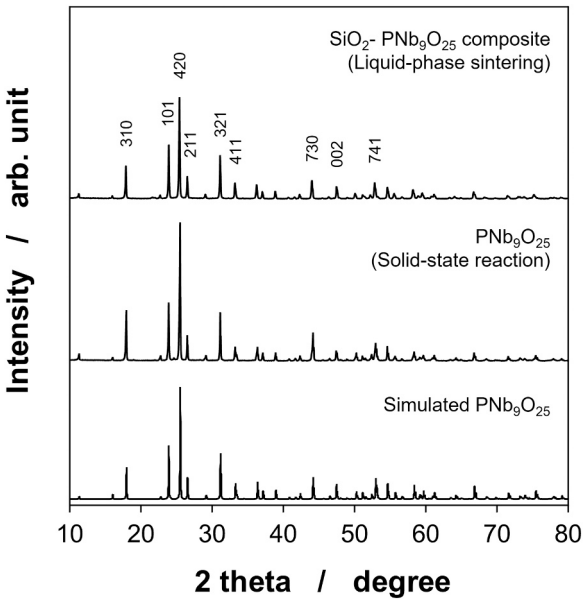

Fig. 3. Powder XRD patterns of the samples synthesized via the solid-state reaction and liquid-phase sintering.

grains. In the liquid-phase sintering system designed in this study, PNb_9O_{25} is synthesized through the reaction between the 50SiO_2–50 P_2O_5 glass and Nb_2O_5, with SiO_2 remaining as a residual phase at the grain boundaries. During sintering, the consumption of P^{5+} ions from the glass for the formation of PNb_9O_{25} increased the viscosity of the SiO_2-rich phase, which likely suppressed the growth of PNb_9O_{25} grains by acting as a barrier phase. A similar phenomenon has been reported during glass crystallization, where the consumption of crystal-forming components from the glass during crystallization increases the viscosity of the remaining glass phase. As a result, a high-viscosity phase forms around the precipitated crystals, acting as a barrier phase that restricts further grain growth [18,19]. To visualize ion diffusion at the 50SiO_2–50 P_2O_5 glass–Nb_2O_5 interface, the 50SiO_2–50 P_2O_5 glass compact and Nb_2O_5 compact were sintered in contact at 1300 °C for 5 h, as shown in Figure S2**(a)**. Figure S2**(b)** shows the energy dispersive X-ray spectrometry (EDS) line scan in SEM across the 50SiO_2–50 P_2O_5 glass–Nb_2O_5 interface, revealing that P diffused approximately 1 μm into the Nb_2O_5 side, whereas Si shows negligible diffusion. These results indicate that P migrates from the glass into Nb_2O_5 during sintering, while Si remains in the glass phase.

The elemental mappings of the sample synthesized using liquid-phase sintering, obtained by SEM-EDS, are shown in Fig. 4**(c)**. The

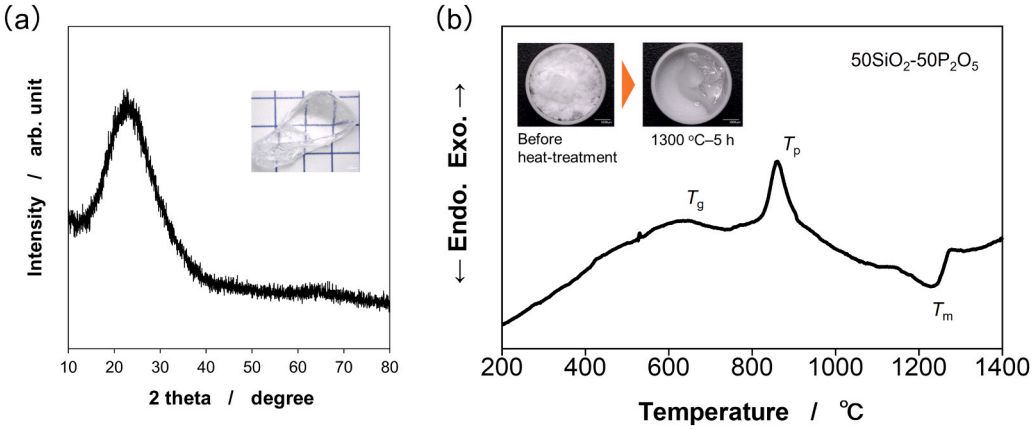

Fig. 2. (a) XRD Pattern and (b) DTA profile for the 50SiO_2–50 P_2O_5 precursor glass.

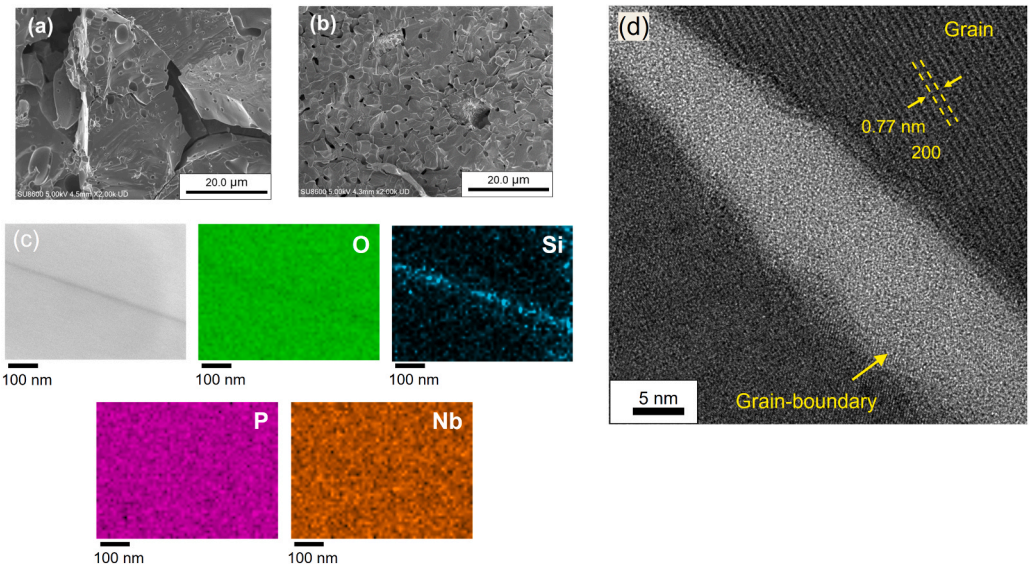

Fig. 4. SEM images of the fracture surface of PNb_9O_{25} synthesized via the (a) solid-state reaction and (b) liquid-phase sintering. () SEM image and corresponding elemental mappings of the grain boundary in PNb_9O_{25} synthesized via liquid-phase sintering. (d) HRTEM image of the grain boundary and grain in the sample synthesized via liquid-phase sintering.

grains consist of P, Nb, and O, whereas the grain boundary contains Si and O. P and Nb detected at the grain boundary were considered to originate from grains overlapping the grain boundary, suggesting that the grain boundary is mainly composed of Si and O. Calculations of the oxygen atomic fractions indicate that PNb_9O_{25} (≈71.4 at%) contains a higher proportion of oxygen than SiO_2 (≈66.7 at%). Thus, in the elemental mapping of O, the bright regions correspond to PNb_9O_{25}, while the dark regions correspond to SiO_2. Fig. 4**(d)** shows high-resolution transmission electron microscopy (HRTEM) image of the region around a grain boundary in the liquid-phase sintered sample. In the grain areas, lattice fringes associated with the crystals were observed. In contrast, lattice fringes in the grain boundary area were unclear, suggesting the presence of an amorphous phase. The interplanar distances are measured to be 0.77 nm on the HRTEM image, matching very well with the 200 crystallographic plane of PNb_9O_{25}.

The Nb 3d X-ray photoelectron spectroscopy (XPS) spectra of PNb_9O_{25} samples synthesized thorough the solid-state reaction and liquid-phase sintering are shown in Fig. 5. Whereas the sample synthesized using the solid-state reaction contains both peaks corresponding to Nb^{4+} and Nb^{5+}, the sample synthesized via liquid-phase sintering exhibits only the peak corresponding to Nb^{5+}. In the photographs of the samples (insets in Fig. 5), the central region of the sample synthesized via the solid-state reaction shows a dark blue coloration, which is consistent with the Nb 3d XPS spectra. This indicates that oxygen vacancies were generated during solid-state reaction, leading to the reduction of Nb^{5+} to Nb^{4+} ions. The generation of one oxygen vacancy is counterbalanced by the incorporation of two Nb^{4+} ions into the crystal structure to maintain electroneutrality. The corresponding reaction could be described using the Kröger–Vink defect notation.

$$2Nb^{5+} + O_O^{\times} \rightarrow 2Nb^{4+} + V_O^{\cdot\cdot} + 1/2O_2 \quad (g) \tag{1}$$

In contrast, the reduction of Nb ions was suppressed in the sample synthesized via liquid-phase sintering, suggesting that this sample contains fewer oxygen vacancies than the sample synthesized through the solid-state reaction. Previous studies have investigated oxygen diffusion behavior using ^{18}O tracer in crystalline–amorphous microstructures, revealing that amorphous layers act as barriers that suppress oxygen migration [20]. Similarly, herein, the high-viscosity SiO_2-rich phase surrounding the grains is considered to act as a barrier that suppresses oxygen migration and hinders oxygen release. Therefore, the high-viscosity glass phase can restrict oxygen permeation and protect Nb ions against reduction.

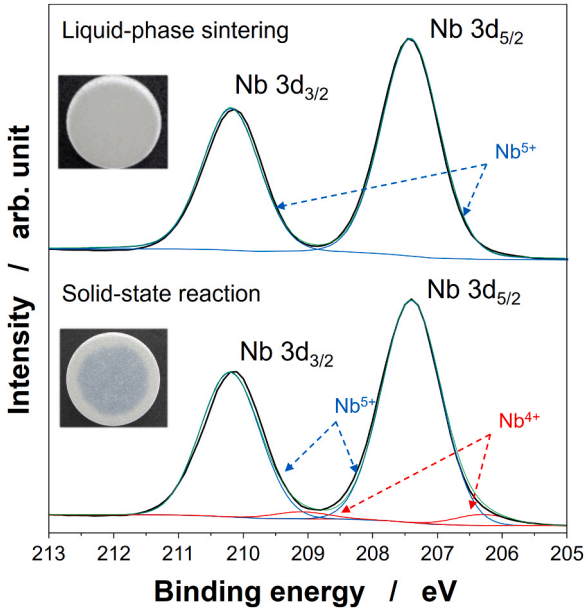

Fig. 5. Nb 3d XPS spectra of PNb_9O_{25} synthesized via the solid-state reaction and liquid-phase sintering. The insets show the photographs of the samples.

3.3. *Dielectric properties of PNb_9O_{25}*

Fig. 6**(a)** shows the dielectric constant (ε) and dielectric loss (tan δ) as a function of frequency at room temperature. In the sample synthesized via liquid-phase sintering, a stable ε and low tan δ are observed below approximately 100 kHz. Above this frequency, ε decreases while tan δ increases. This dielectric behavior is a typical Deby-like (Maxwell-Wagner) dielectric response [21–23]. In contrast, the sample synthesized via the solid-state reaction showed an increase in both ε and tan δ at low frequencies. The temperature dependence of ε and tan δ are shown in Figure S3**(a)–(d)**. In the sample synthesized via the solid-state

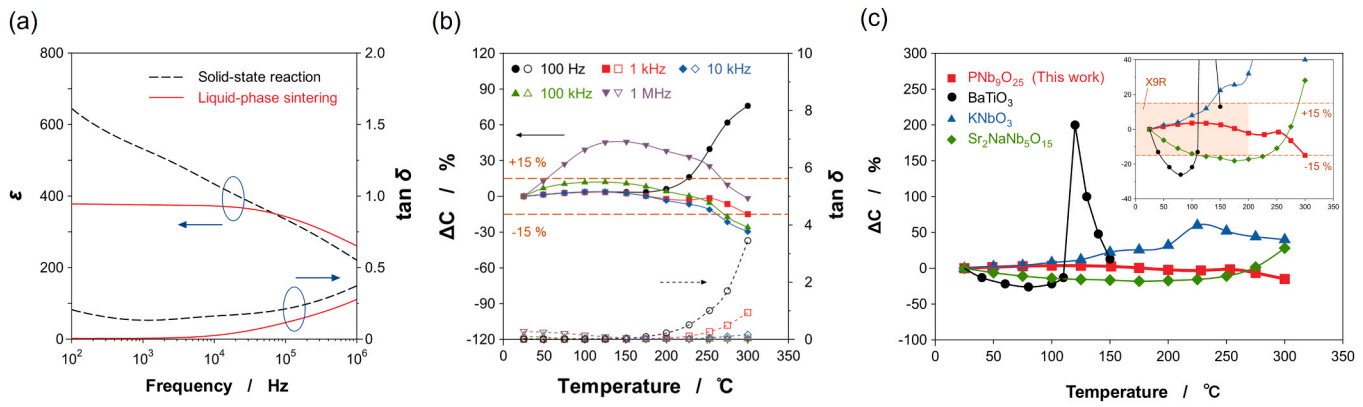

Fig. 6.. (a) Dielectric constant and dielectric loss as a function of frequency at room temperature for PNb_9O_{25} synthesized via the solid-state reaction and liquid-phase sintering. (b) Capacitance variation rate ⊿C ((C_T − $C_{25\ °C}$) / $C_{25\ °C}$) and dielectric loss as a function of temperature for PNb_9O_{25} synthesized through liquid-phase sintering. (c) Comparison of the capacitance variation rates (⊿C) of various dielectric materials [29–31].

reaction, a broad dielectric peak appears at approximately 210 °C in ε–T, and a corresponding relaxation peak appears at approximately 250 °C in tan δ–T. This frequency-dependent dielectric response, as well as the increase in both ε and tan δ at low frequencies, can be attributed to space charge polarization and increased conductivity [24–26], both of which are closely related to oxygen vacancies. Such a behavior has been reported in various perovskite materials and PNb_9O_{25} [8,27,28]. In the sample synthesized via liquid-phase sintering, a broad and poorly defined dielectric peak was observed at approximately 250 °C, while the corresponding relaxation peak was not clearly observed. The difference in the appearance and position of the dielectric peak observed in the sample synthesized via liquid-phase sintering may be attributed to fewer oxygen vacancies and improved grain-boundary structure.

Fig. 6**(b)** shows the capacitance variation rate (⊿C) and tan δ as a function of temperature for PNb_9O_{25} synthesized via liquid-phase sintering. For practical application as a capacitor, ⊿C should be within 15% [29]. The obtained results indicate that the sample synthesized via liquid-phase sintering meets this requirement over a wide temperature range of 25–250 °C or more at the frequencies below 100 kHz, with the corresponding tan δ being less than 0.3. Fig. 6**(c)** summarizes the ⊿C at 1 kHz for previously reported dielectric materials [29–31]. The degradation in the capacitance stability of dielectric materials at elevated temperatures can be attributed not only to the structural phase transition from the ferroelectric phase to the paraelectric phase but also to space charge polarization and an increase in electrical conductivity increase, which are closely related to oxygen vacancies [8,27,28]. Meanwhile, PNb_9O_{25} synthesized via our liquid-phase sintering approach maintains ⊿C within ±15% up to 300 °C, exhibiting better capacitance stability at high temperatures than other dielectric materials. This can be attributed to PNb_9O_{25} not undergoing structural phase transitions, as well as to the suppression of oxygen vacancies by the amorphous phase at the grain boundaries.

3.4. *Electrical properties of PNb_9O_{25}*

The electrical properties of PNb_9O_{25} synthesized through the solid-state reaction and liquid-phase sintering were investigated using complex impedance spectroscopy. Polycrystalline materials typically show both grain and grain boundary effects with different time constants, resulting in two successive semicircles in a complex plane plot (Z'' vs. Z'). Figure S4 shows the complex plane (Nyquist) plots of Z'' versus Z' measured at several temperatures. The sample synthesized via liquid-phase sintering showed two overlapping semicircles at 302 °C. In the two overlapping semicircles, the high-frequency semicircle corresponds to the bulk resistance (R_b), while the low-frequency semicircle corresponds to the grain-boundary resistance (R_{gb}) [32]. At the other measurement temperatures, a distinct broadening of the semicircles was observed for both samples. This broadening can be attributed to the overlap of the two semicircles caused by small time constants.

In most cases, the experimental data reveal a deviation from ideal R–C behavior, which is observed as a deformation of the semicircles. This deformation of the semicircles has been reported to be caused by inhomogeneities in the local distribution of defects and the presence of ionic charge carriers. For example, high-purity quartz glass with inappreciable electronic and ionic conductivity shows an ideal semicircle [33]. In contrast, lithium borate glasses with appreciable ionic conductivity exhibit a deformed semicircle [33]. Following a previous report, the bulk and grain-boundary resistance of the samples were analyzed using R-CPE (Constant Phase Element) equivalent circuits [33]. The DC conductivity (σ) of the samples was calculated based on the resistance values obtained from the Nyquist plots (Fig. 7**(a)**). The conductivity follows the Arrhenius equation.

$$\sigma = A\ \exp(-E_a/k_BT) \tag{2}$$

where A is the pre-exponential factor, k_B is Boltzmann's constant, T is the temperature, and E_a is the activation energy of the conduction process. For the sample synthesized via the solid-state reaction, the activation energies of bulk conduction ($E_{a(b)}$) and grain-boundary conduction ($E_{a(gb)}$) were 0.34 and 0.65 eV, respectively. For the sample synthesized via liquid-phase sintering, the corresponding energies were 0.38 and 0.89 eV, respectively. These E_a values are in good agreement with previously reported activation energies for the single- and doubly-ionized oxygen vacancies, which are typically in the ranges of 0.1–0.5 and 0.6–1.2 eV, respectively [34,35]. The values of $E_{a(b)}$ for the samples synthesized via the solid-state reaction and liquid-phase sintering are nearly identical, indicating that the underlying charge-transport mechanisms within the bulk are essentially the same. In contrast, $E_{a(gb)}$ of the sample synthesized via liquid-phase sintering is higher than that of the sample synthesized through the solid-state reaction, suggesting that the amorphous–crystalline microstructure would act as a barrier phase for oxygen-vacancy formation.

Fig. 7**(b)** compares the electrical conductivity of PNb_9O_{25} synthesized in this study with that of other dielectric materials for high-temperature applications [8,35–38]. The electrical conductivity of PNb_9O_{25} considerably depends on the microstructure. In our liquid-phase sintering method, which utilizes interfacial reactions between the glass and oxide, grain refinement and the formation of an amorphous–crystalline microstructure occur simultaneously. Therefore, the sample synthesized via liquid-phase sintering exhibits better insulating properties than samples prepared via other synthesis methods, which was attributed to microstructural features. Moreover, the electrical conductivity of PNb_9O_{25} synthesized through liquid-phase

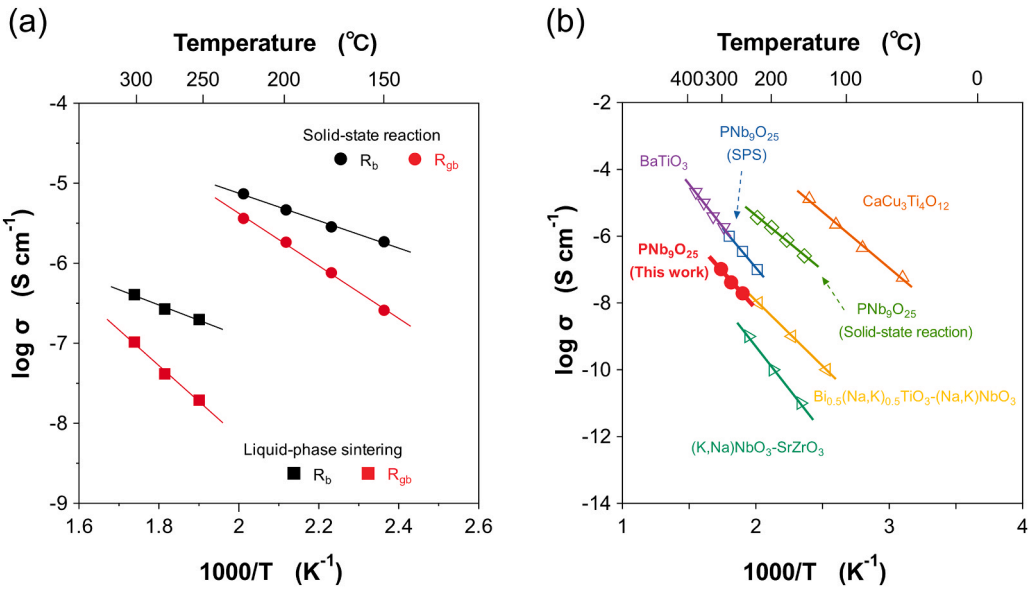

Fig. 7.. (a) Temperature dependence of the DC conductivity of PNb_9O_{25} synthesized via the solid-state reaction and liquid-phase sintering. (b) DC conductivity of various dielectric materials for high-temperature applications [8,35–38].

sintering is comparable to or lower than that of other promising dielectric materials, such as $(K,Na)NbO_3$-$SrZrO_3$ and $Bi_{0.5}(Na,K)_{0.5}TiO_3$-$(Na,K)NbO_3$, indicating its potential as a dielectric material for high-temperature dielectric applications.

4. Conclusion

Herein, SiO_2–PNb_9O_{25} composites were synthesized using our liquid-phase sintering method from $50SiO_2$–$50\ P_2O_5$ glass and Nb_2O_5, and their chemical states, microstructure, and dielectric and electrical properties were investigated. Compared with PNb_9O_{25} synthesized via a conventional solid-state reaction, PNb_9O_{25} synthesized via our liquid-phase sintering method showed higher densification, which was attributed to the effect of capillary forces induced by molten $50SiO_2$–$50\ P_2O_5$ glass during sintering. The interfacial reaction between molten $50SiO_2$–$50\ P_2O_5$ glass and Nb_2O_5 promoted the formation of PNb_9O_{25} through the diffusion of P^{5+} ions from the glass phase, with the SiO_2–rich amorphous phase suppressing grain growth, inhibiting Nb reduction, and restricting the formation of oxygen vacancies. Owing to the effects of an amorphous–crystalline microstructure, PNb_9O_{25} maintained capacitance stability within ±15% and DC conductivity below 10^{-7} S cm^{-1} up to 300 °C. These results indicate that the strategic utilization of glass–oxide interfacial reactions in liquid-phase sintering is an effective approach for controlling microstructure, enhancing dielectric properties, and improving insulating characteristics. PNb_9O_{25} synthesized via our liquid-phase sintering method is a promising candidate for high-temperature dielectric applications.

Appendices

Supplementary data associated with this article is available from ScienceDirect or from the author.

CRediT authorship contribution statement

Keisuke SHIMAMURA: Writing – original draft, Visualization, Supervision, Project administration, Investigation, Conceptualization. **Daisuke OGAWA:** Investigation. **Chihaya FUJIWARA:** Investigation. **Hiromasa NAMIKI:** Writing – review & editing, Investigation. **Naoki TACHIBANA:** Writing – review & editing, Investigation.

Declaration of Competing Interest

The authors declare that they have no known competing financial interests or personal relationships that could have appeared to influence the work reported in this paper.

Appendix A. Supporting information

Supplementary data associated with this article can be found in the online version at doi:10.1016/j.mtcomm.2026.115539.

Data availability

Data will be made available on request.

References

[1] S. Pattipaka, Y. Lim, Y.H. Son, et al., Ceramic-based dielectric materials for energy storage capacitor applications, materials 17 (2024) 2277, https://doi.org/10.3390/ma17102277.
[2] A.R. Jayakrishnan, J.P.B. Silva, K. Kamakshi, et al., Are lead-free relaxor ferroelectric materials the most promising candidates for energy storage capacitors? Prog. Mater. Sci. 132 (2023) 101046 https://doi.org/10.1016/j.pmatsci.2022.101046.
[3] B. Fan, F. Liu, G. Yang, et al., Perspectives and challenges in multilayer ceramic capacitors for next generation electronics, J. Mater. Chem. C. 7 (2019) 9782–9802, https://doi.org/10.1039/C9TC02921D.
[4] B. Fan, F. Liu, G. Yang, et al., Dielectric materials for high-temperature capacitors, IET Nanodielectr 1 (2018) 32–40, https://doi.org/10.1049/iet-nde.2018.0002.
[5] T. Schulz, V.K. Veerapandiyan, T. Gindel, et al., Hexavalent (*Me* - W/Mo)-modified (Ba,Ca)TiO_3-Bi(Mg,*Me*)O_3 perovskites for high-temperature dielectrics, J. Am. Ceram. Soc. 103 (2020) 6881–6892, https://doi.org/10.1111/jace.17403.
[6] X. Chen, D. Ma, G. Huang, et al., $K_{0.5}Na_{0.5})NbO_3$–$Bi(Zn_{0.5}Zr_{0.5})O_3$ perovskite ceramics: high relative permittivity, low dielectric loss and good thermal stability, Ceram. Int. 41 (2015) 13883–13886, https://doi.org/10.1016/j.ceramint.2015.07.118.
[7] M. Acosta, J. Zang, W. Jo, J. Rödel, High-temperature dielectrics in $CaZrO_3$-modified $Bi_{1/2}Na_{1/2}TiO_3$-based lead-free ceramics, J. Eur. Ceram. Soc. 32 (2012) 4327–4334, https://doi.org/10.1016/j.jeurceramsoc.2012.06.011.
[8] J. Fu, High and temperature-stable dielectric constants in PNb_9O_{25} ceramic, J. Am. Ceram. Soc. 105 (2022) 3740–3745, https://doi.org/10.1111/jace.18414.
[9] J.L. Waring, R.S. Roth, Tetragonal phases of the general type $10M_2O_5.90M'_2O_5$ apparently isostructural with $Ta_2O_5.2Nb_2O_5$, Acta Crystallogr. 17 (1964) 455–456, https://doi.org/10.1107/S0365110X64001049.
[10] R.S. Roth, A.D. Wadsley, S. Andersson, The crystal structure of PNb_9O_{25} ($P_2O_5.9Nb_2O_5$), Acta Crystallogr. 18 (1965) 643–647, https://doi.org/10.1107/S0365110X65001500.

[11] K. Shimamura, J. Fu, Dielectric properties of PNb_9O_{25}–$GeNb_{18}O_{47}$ ceramics, J. Ceram. Soc. Jpn. 131 (2023) 549–554, https://doi.org/10.2109/jcersj2.22158.
[12] S. Liu, B. Shen, H. Hao, J. Zhai, Glass–ceramic dielectric materials with high energy density and ultra-fast discharge speed for high power energy storage applications, J. Mater. Chem. C. 7 (2019) 15118–15135, https://doi.org/10.1039/C9TC05253D.
[13] W. Zhang, S. Xue, S. Liu, et al., Structure and dielectric properties of $Ba_xSr_{1-x}TiO_3$-based glass ceramics for energy storage, J. Alloy. Compd. 617 (2014) 704–745, https://doi.org/10.1016/j.jallcom.2014.08.077.
[14] S. Xiu, B. Shen, J. Zhai, The effects of MnO_2 addition on the structure and dielectric properties of the strontium barium niobate glass-ceramics, Mater. Res. Bull. 95 (2017) 349–353, https://doi.org/10.1016/j.materresbull.2017.08.008.
[15] X. Lü, H. Lin, Investigation on low-temperature reactive viscous flow sintering behavior of lanthanum-borate glass-ceramic with $BaTi_4O_9$ ceramic filler, J. Eur. Ceram. Soc. 40 (2020) 4035–4046, https://doi.org/10.1016/j.jeurceramsoc.2020.05.025.
[16] K. Kobayashi, T.S. Suzuki, Free analysis and visualization programs for electrochemical impedance spectroscopy coded in python, Electrochemistry 89 (2021) 218–222, https://doi.org/10.5796/electrochemistry.21-00010.
[17] R.M. German, P. Suri, S.J. Park, Review: liquid phase sintering, J. Mater. Sci. 44 (2009) 1–39, https://doi.org/10.1007/s10853-008-3008-0.
[18] C. Bocker, S. Bhattacharyya, T. Höche, C. Rüssel, Size distribution of BaF_2 nanocrystallites in transparent glass ceramics, Acta Mater. 57 (2009) 5956–5963, https://doi.org/10.1016/j.actamat.2009.08.021.
[19] C. Bocker, C. Rüssel, I. Avramov, Transparent nano crystalline glass-ceramics by interface controlled crystallization, Int. J. Appl. Glass Sci. 4 (2013) 174–181, https://doi.org/10.1111/ijag.12033.
[20] E. Aschauer, T. Wojcik, P. Polcik, et al., Ultra-high oxidation resistance of nano-structured thin films, Mater. Des. 201 (2021) 109499, https://doi.org/10.1016/j.matdes.2021.109499.
[21] T. Prodromakis, C. Papavassiliou, Engineering the Maxwell–Wagner polarization effect, Appl. Surf. Sci. 225 (2009) 6989–6994, https://doi.org/10.1016/j.apsusc.2009.03.030.
[22] P. Thongbai, J. Jumpatam, B. Putasaeng, et al., Microstructural evolution and Maxwell–Wagner relaxation in $Ca_2Cu_2Ti_{4-x}Zr_xO_{12}$: the important clue to achieve the origin of the giant dielectric behavior, Mater. Res. Bull. 60 (2014) 695–703, https://doi.org/10.1016/j.materresbull.2014.09.045.
[23] Z. Pheng, J. Wang, X. Lei, et al., Colossal dielectric response in $CdAl_xCu_{3-x}Ti_4O_{12}$ perovskite ceramics, Mater. Chem. Phys. 258 (2021) 123940, https://doi.org/10.1016/j.matchemphys.2020.123940.
[24] E. Haily, L. Bih, A. El Bouari, et al., Effect of BaO–Bi_2O_3–P_2O_5 glass additive on structural, dielectric and energy storage properties of $BaTiO_3$ ceramics, Mater. Chem. Phys. 241 (2020) 122434, https://doi.org/10.1016/j.matchemphys.2019.122434.
[25] C. Elissalde, J. Ravez, Ferroelectric ceramics: defects and dielectric relaxations, J. Mater. Chem. 11 (2001) 1957–1967, https://doi.org/10.1039/B010117F.
[26] E. Haily, L. Bih, A. El Bouari, et al., Structural, optical, and dielectric properties of the BaO–TiO_2–P_2O_5 glasses, J. Aust. Ceram. Soc. 56 (2020) 1467–1479, https://doi.org/10.1007/s41779-020-00473-1.
[27] O. Bidault, P. Goux, M. Kchikech, M. Belkaoumi, M. Maglione, Space-charge relaxation in perovskites, Phys. Rev. B 49 (1994) 7868–7873, https://doi.org/10.1103/PhysRevB.49.7868.
[28] J.S. Kim, B.C. Choi, J.W. Chung, et al., Low-frequency dielectric property and impedance spectroscopy of bismuth-lanthanum-titanate ceramics with Nb doping, J. Korean Phys. Soc. 52 (2008) 410–414, https://doi.org/10.3938/jkps.52.410.
[29] M.-J. Pan, C.A. Randall, A brief introduction to ceramic capacitors, IEEE Electr. Insul. Mag. 26 (2010) 44–50, https://doi.org/10.1109/MEI.2010.5482787.
[30] H. Birol, D. Damjanovic, N. Setter, Preparation and characterization of $KNbO_3$ ceramics, J. Am. Ceram. Soc. 88 (2005) 1754–1759, https://doi.org/10.1111/j.1551-2916.2005.00347.x.
[31] J.P. Tidey, U. Dey, A.M. Sanchez, et al., Structural origins of dielectric anomalies in the filled tetragonal tungsten bronze $Sr_2NaNb_5O_{15}$, Commun. Mater. 5 (2024) 71, https://doi.org/10.1038/s43246-024-00508-1.
[32] J.T.S. Irvine, D.C. Sinclair, A.R. West, Electroceramics: characterization by impedance spectroscopy, Adv. Mater. 2 (1990) 132–138, https://doi.org/10.1002/adma.19900020304.
[33] M.R. Shoar Abouzari, F. Berkemeier, G. Schmitz, D. Wilmer, On the physical interpretation of constant phase elements, Solid. State Ion. 180 (2009) 922–927, https://doi.org/10.1016/j.ssi.2009.04.002.
[34] N. Zhao, P. Liang, L. Wei, L. Yang, Z. Yang, Synthesis and dielectric anomalies of $CdCu_3Ti_4O_{12}$ ceramics, Ceram. Int. 41 (2015) 8501–8510, https://doi.org/10.1016/j.ceramint.2015.03.057.
[35] H.M. Kotb, M.M. Ahmad, A. Alshoaibi, K. Yamada, Dielectric response and structural analysis of (A^{3+}, Nb^{5+}) cosubstituted $CaCu_3Ti_4O_{12}$ ceramics (A: Al and Bi), Materials 13 (2020) 5822, https://doi.org/10.3390/ma13245822.
[36] R. Dittmer, E.-M. Anton, W. Jo, H. Simons, et al., A high-temperature-capacitor dielectric based on $K_{0.5}Na_{0.5}NbO_3$-modified $Bi_{1/2}Na_{1/2}TiO_3$–$Bi_{1/2}K_{1/2}TiO_3$, J. Am. Ceram. Soc. 95 (2012) 3519–3524, https://doi.org/10.1111/j.1551-2916.2012.05321.x.
[37] L. Ben, L. Li, J.H. Harding, et al., Tuning the electrical conductivity of rare earth-doped $BaTiO_3$ using Gd_2O_3 as an exemplar, Open. Ceram. 9 (2022) 100250, https://doi.org/10.1016/j.oceram.2022.100250.
[38] S. Aman, K. Kubo, H. Akiba, and D. Inagawa, Core–shell structure and dielectric properties of $(K_{0.5}Na_{0.5})NbO_3$–$SrZrO_3$ for high-temperature capacitors, Jpn. J. Appl. Phys. 55 (2016) 10TB08, https://doi.org/10.7567/JJAP.55.10TB08.